

Product-state control in barium

Rekishu Yamazaki* and D. S. Elliott†

School of Electrical and Computer Engineering and Department of Physics, Purdue University, West Lafayette, Indiana 47907, USA

(Received 30 September 2005; published 15 February 2006)

We report photoionization measurements that help us interpret mechanisms leading to the control of the branching ratio for resonantly enhanced, two-color, two-photon ionization experiments. We measure intermediate state populations and photoelectron angular distributions to explore the ionization dynamics. Our measurements support the interpretation that ac Stark shifts are the primary mechanism of the product state control previously observed in a similar experimental setup. We discuss the role of interference in the ionization continuum and the effect of the ac Stark shift on the product state control.

DOI: [10.1103/PhysRevA.73.023415](https://doi.org/10.1103/PhysRevA.73.023415)

PACS number(s): 32.80.Rm, 32.80.Qk

I. INTRODUCTION

Since the introduction of the laser, it has been of great interest to utilize this tool as a means of controlling chemical reactions, selectively breaking specific molecular bonds while leaving others intact. Many of the early attempts of selective bond breaking in molecules suffered from the coupling within molecules that redistributed the absorbed energy, causing other bonds to break. Recently, coherent control processes have been explored, providing an additional degree of freedom for controlling the branching ratio of photofragments. In this field, the laser coherence properties are used explicitly to steer the molecule into specific quantum mechanical states. Different schemes in coherent control of photofragment branching ratios include timing control of sequential laser pulses [1], pulse shaping of ultrashort pulses using learning and feedback control [2,3], and multi-pathway quantum interferences [4–7]. Most of the photofragmentation experiments require high laser intensities, and the control could be the result of combinations of many different phenomena, including saturation, Stark shifts, multi-photon reactions, quantum interferences, etc. Key for the optimization of the control in such experiments is our understanding of the role of different effects that can take place in high laser intensity experiments.

In our previous reports [7] on photoionization of atomic barium, we successfully demonstrated control of the electronic excitation of the Ba^+ core using two resonant laser fields. In that demonstration, we set up two individual two-color, two-photon ionization processes, each enhanced by a near resonance of one of the field frequency components with an intermediate state of the barium atom. For each ionization process, absorption of one photon from each field component excites the ground state electron into the continuum, which is characterized by three different ionization channels, leaving the barium core in $6s^2S_{1/2}$ ground state or the excited $5d^2D_{3/2}$ or $5d^2D_{5/2}$ state. As we scanned one of the laser frequencies across the intermediate state resonance, while holding the other laser frequency constant, we ob-

served a strong asymmetry in the ionization yield for all three different ionization channels. The observed control of the branching ratio to the $6s$ core state varied from 95% to 58%. Our initial interpretation of the highly asymmetric spectra that we observed was in terms of an interference between the two optical pathways leading to the continuum state.

Two groups subsequently reported theoretical investigations related to our experimental observations. Nakajima *et al.* [8] studied two-pathway, two-photon ionization in atomic calcium using density matrix calculations, and Luc-Koenig *et al.* [9] carried out a set of numerical calculations using an adiabatic approximation, with the atomic parameters obtained from *jj*-coupled eigenchannel *R*-matrix and multi-channel quantum defect theory (MQDT). These studies showed that the dominant influence on the ionization yield was that of the ac Stark shift of the barium ground state, rather than the multi-path quantum interference. In the present work, we advance the study of the role of these different effects in the product state control in barium photoionization using measurements of (1) the residual intermediate state population and (2) the angular distribution of the photoelectrons. We present evidence that supports the interpretation that, in this case, the Stark shift is indeed the dominant mechanism leading to the asymmetric photoionization line shapes and control of the branching ratio. We also apply the theoretical models of Refs. [8,9] in order to explore other conditions that might lead to an enhanced role of the two-pathway interference and discuss these in Sec. V.

II. DESCRIPTION OF THE INTERFERENCE AND THE ac STARK SHIFT

We show in Fig. 1 an energy level diagram containing the states of atomic barium that are relevant in our experiment. Two laser field components, of frequencies ω_1 (~ 554 nm in wavelength) and ω_2 (~ 307 nm in wavelength), are tuned near the transition frequencies, $\omega_a/2\pi c = 18\,060.3$ cm^{-1} and $\omega_b/2\pi c = 32\,547.1$ cm^{-1} , for excitation of the barium ground state to the intermediate $6s6p^1P_1$ and $6s7p^1P_1$ states, respectively. Ionization to the continuum state of energy $\varepsilon = \hbar(\omega_1 + \omega_2) \approx 50\,607.4$ cm^{-1} can be achieved via two pathways, each resonantly enhanced by one of these intermediate states.

*Electronic address: yamazaki@purdue.edu

†Electronic address: elliottd@purdue.edu

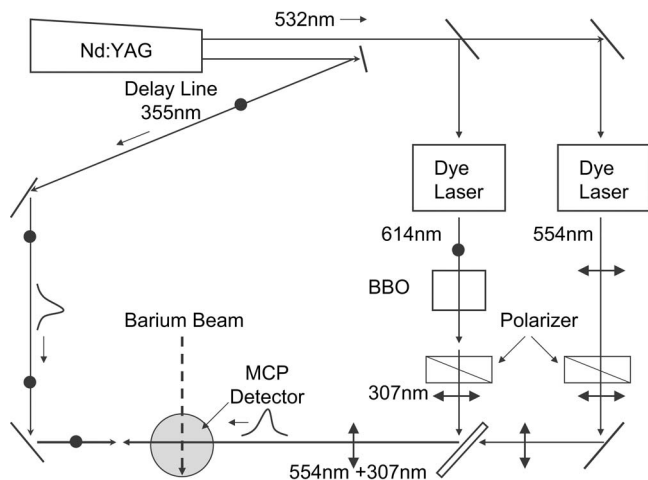


FIG. 2. Experimental setup. The second harmonic output of the Nd:YAG laser pumps two dye lasers, which generate tunable pulses at $\lambda=554$ nm and, through second harmonic generation in the BBO crystal, $\lambda=307$ nm. These beams intersect the beam of barium atoms, and we detect the photoelectrons using the MCP detector. The temporally delayed third harmonic output of the Nd:YAG laser at $\lambda=355$ nm allows us to determine any residual intermediate state population.

the 614 nm beam, producing about $50 \mu\text{J}$ at 307 nm, in a type I phase-matched second-harmonic generating beta-barium borate (BBO) crystal. We improve the polarization and transverse mode of the two beams using Glan laser polarizers (aligned to within ~ 3 mrad of each other) and spatial filters, respectively, and collimate these beams before combining them using a dielectric beam combiner. We monitor the frequencies of the two-color field during the experiment with a wavemeter with an accuracy of 0.02 cm^{-1} . The durations of the laser pulses are about 5–6 ns (FWHM), and we match the timing of their peaks to within 0.5 ns using a fast photodiode. The two-color laser pulses are in a near-Gaussian transverse mode of radius w_0 (radius at which the intensity drops to e^{-2} of the on-axis intensity) $\sim 300 \mu\text{m}$ at the interaction region. We chose this beam size in order to be consistent with our previous work [7] and also to allow a sufficient signal strength. Although matching wave fronts of the two laser beams is not necessary (as it was in most of our other observations of coherent control processes [11,13,14]), we align the beams carefully to assure good spatial overlap. We employ two methods to achieve this: we center the beams on two pinholes positioned before and after the interaction region; and we maximize the two-color photoionization signal. We estimate the peak intensity of the two laser field components to be $5.3 \times 10^7 \text{ W/cm}^2$ for the 554 nm laser pulse and $6.6 \times 10^6 \text{ W/cm}^2$ at 317 nm, when operated at typical pulse energies of 400 and $50 \mu\text{J}$, respectively.

We generate the atomic barium beam using an effusive oven heated to a typical temperature of $510 \text{ }^\circ\text{C}$. The background pressure inside the vacuum chamber is 2×10^{-8} torr. We monitor the temperature of the oven with thermocouple temperature probes mounted on the front and back of the oven. The laser beams and the barium beam intersect one another at right angles, and the diameter of the barium beam

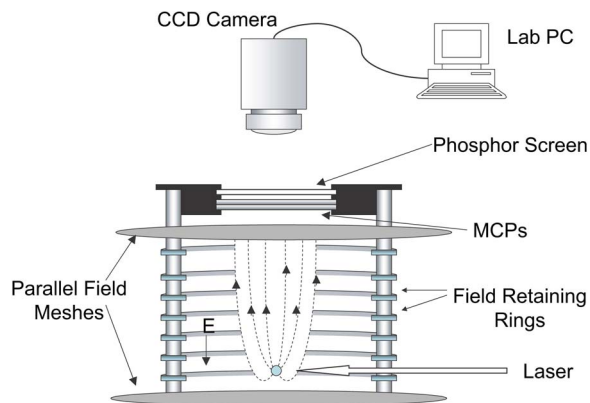


FIG. 3. (Color online) MCP detector assembly used in the experiment. The interaction region, defined by the intersection of the laser beams and the barium atomic beam, is positioned between two parallel field meshes, to which we apply a 400 V potential difference. The photoelectrons follow a parabolic trajectory towards the upper mesh. Those electrons that are transmitted through the mesh are amplified in the microchannel plate (MCP) electron multiplier and produce a bright spot on the phosphor screen. We record and accumulate the photoelectron image using a CCD camera interfaced to a laboratory PC.

at the interaction region is about 1 mm. We estimate the atomic density of the barium in the interaction region to be $5.7 \times 10^6 \text{ cm}^{-3}$. We cancel the earth's magnetic field to within 10 mG in the interaction region using three orthogonal pairs of magnet coils positioned outside the vacuum system.

We show a schematic diagram of the photoelectron detector assembly in Fig. 3. The interaction region is positioned between two plane parallel stainless steel meshes, above which we position a microchannel plate/phosphor screen assembly. Each mesh, consisting of 1 mil diameter wires spaced by 10 mil, is about 20 cm in diameter. One is located 10 cm above, the other 0.5 cm below, the interaction region. The meshes are held at a constant potential difference of about 400 V, creating a uniform electric field in the region between the meshes. We reduce the field nonuniformity in the electron flight region by positioning field retaining rings around the flight region with appropriate voltages applied to each ring. The uniform electric field accelerates the photoelectrons ejected from the atoms upward, such that the photoelectrons make parabolic trajectories toward the MCP detector assembly.

Electrons transmitted by the upper mesh are amplified (typical gain of 10^6) in the microchannel plate multiplier (MCP) and strike the phosphor screen directly above the MCP, producing a bright spot (lifetime of about $500 \mu\text{s}$) on the screen. We capture the phosphorescence image with an asynchronous reset CCD camera and store it in a laboratory computer (PC) with a frame grabber. For each laser pulse, we detect as many as 100 photoelectrons, and we accumulate an image over 500–3000 laser pulses to decrease the statistical fluctuations. Each electron incident on the MCP illuminates an average of 3–4 pixels in the CCD camera, and we process the images using a threshold detection and pixel counting algorithm to locate the center of mass of the electron and

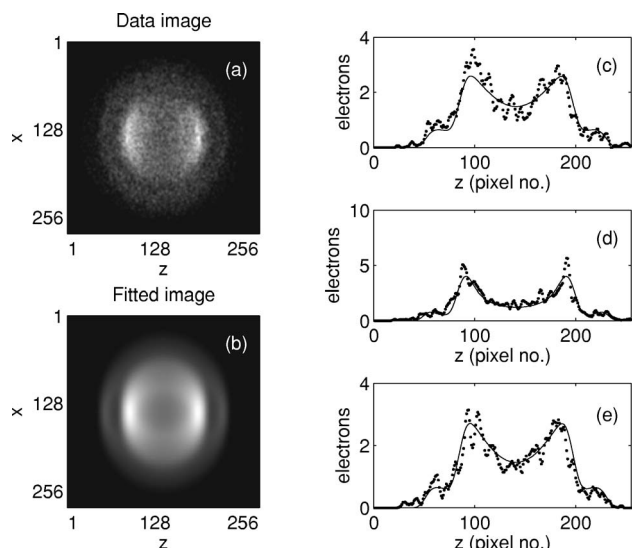


FIG. 4. (a) Image captured with the MCP detector in x - z spatial coordinate. For purposes of this figure, we convolve the data over a square window of area 4 pixels by 4 pixels to smooth its rapid fluctuations. The outer (inner) ring is the outer limit of the fast (slow) electrons. (b) Model image that yields the best fit to the data. The line traces in (c), (d), and (e) show single rows from the image (rows 110, 140, and 170, respectively), with data as circles and the fit as the solid line.

register a single count in the image plane. This technique eliminates multiple counting of electrons and reduces image distortion that might result from gain nonuniformities of the MCP and/or the phosphor screen [11,12].

During an experiment, we fix the pulse energy, E_1 , of the 554 nm beam (100, 200, or 400 μ J per pulse) and the energy, E_2 , and frequency, ω_2 , of the 307 nm beam, tune the frequency, ω_1 , of the 554 nm beam about the atomic resonance frequency, and record the photoelectron image and yield. We show a typical smoothed photoelectron image in Fig. 4(a). The electrons form a distribution in x - z coordinates of the image plane, where x is the direction of propagation of the laser pulses and z is the direction of polarization. Three individual rows of data from this image are shown in Figs. 4(c)–4(e) as the data points. The outer and inner rings in the image correspond to the maximum distance traveled by the fast electrons ($r_{\max}=1.05$ cm for 1.06 eV electrons, which correspond to the $6s$ core state) or slow electrons ($r_{\max}=0.70$ and 0.64 cm for 0.46 and 0.36 eV electrons, respectively, corresponding to the $5d$ core states). The fast and slow electrons can overlap in the central region of this image, so we use an inversion process to separate these two electron images [10]. Inverting the image to E - θ coordinates, where E is the photoelectron energy and θ is the polar angle measured from the z axis, yields two energy bands, one corresponding to the $6s$ core state, the other to the $5d$ core state, that are clearly resolvable. (The energy resolution of our detector is ~ 0.1 – 0.2 eV, limited primarily by the finite size of the interaction region in our experiment. We are therefore unable to resolve the photoelectrons for the $5d_{3/2}$ and $5d_{5/2}$ core states, whose kinetic energies differ by only 0.1 eV.) We integrate over each band in energy and plot the electron

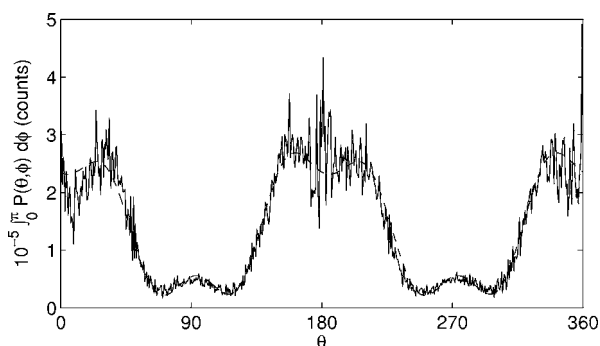


FIG. 5. Photoelectron angular distribution data. The solid line shows the data derived from an image such as that shown in Fig. 4(a), while the dashed line is a fit found by Fourier transforming the data and keeping only the lowest order terms. Each 90° segment of this plot represents data over each of the four quadrants of the image.

count for each band as a function of θ . We show an example in Fig. 5, where each 90° segment represents data in each of the four quadrants of the image. We choose to retain and display the data over the entire (essentially doubled) range of θ so as to be able to identify any effects due to gain nonuniformity of the detector. The dashed line in this figure is the result of a Fourier transformation of the data, in which we retain only the first few terms of the Fourier expansion. Using these fitted expressions for the angular distributions as an initial estimate, we return to the original image data and reconstruct the image for direct comparison, adjusting the amplitudes A_i and B_i , defined in

$$P_{6s}(\theta, \phi) = A_0 + A_2 \cos 2\theta + A_4 \cos 4\theta,$$

$$P_{5d}(\theta, \phi) = B_0 + B_2 \cos 2\theta + B_4 \cos 4\theta \quad (3)$$

to obtain the best fit to the data. These fitted images yield figures such as that shown in Fig. 4(b), as well as the solid lines shown in Figs. 4(c)–4(e), which represent the best fit to the experimental data for individual rows of the image (rows 110, 140, and 170, respectively). We include a small rotation of the image to account for a misalignment of the camera. Overall, we observe very good fits with experimental images for all cases. Finally, we obtain total yields into fast or slow electron channels by summing the fitted images for the $6s$ or $5d$ channels, respectively, over the image plane.

The noise in the image is primarily from two sources. The dominant contribution appears to be consistent with Poisson statistics, as expected from counting single electron events. In addition, we detect about six electrons per laser pulse correlated to the 307 nm pulse, and 0.03 electrons per pulse, which seems to be independent of either of the laser pulses. These noise contributions are likely caused by ionization of background gas, scattering of the laser beams off surfaces within the vacuum system, or dark currents.

The delayed laser pulse that allows us to determine the residual populations of the intermediate $6s6p$ and $6s7p$ states is the vertically polarized third-harmonic output of Nd:YAG laser (355 nm), which propagates counter to the two-color laser pulse with a delay of 12 ns. We chose the timing of the

delay pulse entering the interaction region to be longer than the pulse width of the two-color laser pulse so that the delay pulse does not alter the atomic dynamics during the first pulse. This delay time is greater than or comparable to the lifetimes of the intermediate states, which have been previously measured to be 8.37 and 13.2 ns for $6s6p$ and $6s7p$ [15], respectively. The beam radius w_0 of the delay pulse is $\sim 350 \mu\text{m}$. We used up to 1 mJ of pulse energy in order to generate sufficient delay pulse signal. When the delay pulse is applied, the photoelectron image is a combination of electrons ejected from the two-color field interaction and the delay laser pulse interaction. In order to separate the electron images coming from these different processes we collect three different images for a fixed 554 nm laser frequency. In the first, we apply only the concurrent 554 and 307 nm pulses. This image provides the photoelectron angular distribution and the total ionization yield for each continuum channel. For the second image, we apply the 355 nm delay pulse as well. By taking the difference between the second image (two-color+delay) and the first image (two-color only), we extract the electron image coming only from the delay pulse. Finally, we collect an image for which only the 355 nm delay pulse interacts with the atoms. This last measurement, which amounts to as many as 7 electrons/shot, allows us to correct for ionization of the background gas or noise caused by scattered light at the detector by this pulse. We also observe and correct for a small above-threshold-ionization (ATI) signal (absorption of two 355 nm photons from the $6s6p$ intermediate state), which overlaps with the $6s7p$ delay image. We measure this signal by blocking the 307 nm laser and subtract the signal from the integrated $6s7p$ delay signal.

IV. RESULTS

A. Concurrent resonant pulse photoionization without the delay pulse

We show the dependence of the two-color signal on laser detuning [$\Delta_1 \equiv (\omega_1 - \omega_a)/2\pi c$] in Fig. 6. The data shown are the partial photoionization spectra for three different pulse energies E_1 of the 554 nm laser pulse: 400, 200, and 100 μJ . The energy E_2 of the 307 nm laser pulse is kept constant at 50 μJ for $|\Delta_2| > 2 \text{ cm}^{-1}$, but we reduced E_2 to 30 μJ for smaller $|\Delta_2|$ in order to reduce photoionization through two-photon absorption of the 307 nm beam.

The spectra show asymmetric profiles similar to those that we observed previously [7]. For negative 307 nm laser detuning [$\Delta_2 \equiv (\omega_2 - \omega_b)/2\pi c < 0$], the ionization yield is stronger for positive detuning of the 554 nm laser ($\Delta_1 > 0$). Spectra for $\Delta_2 > 0$ appear as the mirror image of the data shown. The change in the asymmetry of the spectra for different laser intensities is more prominent when the detuning of the 307 nm laser (Δ_2) is large and the effect is more substantial in the fast electrons. For large Δ_2 , as in the spectra with $\Delta_2 = -6.99$ and -3.39 cm^{-1} , the spectra for the fast electron signal are highly asymmetric for high 554 nm pulse energy, but become rather symmetric in the lower intensity regime. The slow electrons, however, show strong asymmetry for all powers of the 554 nm laser pulse.

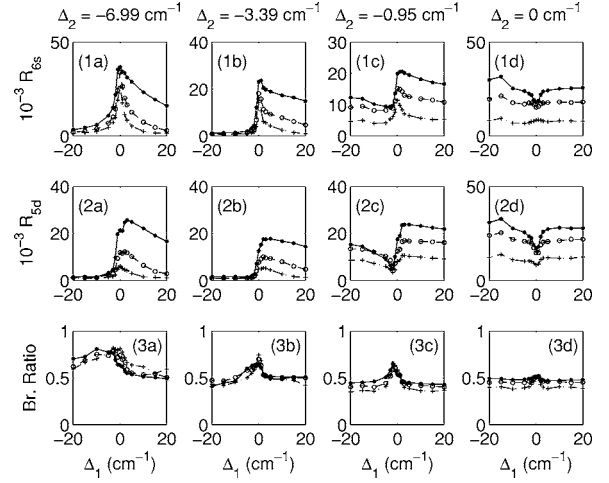


FIG. 6. The asymmetric two-photon ionization signals under a variety of conditions. In each diagram, we show spectra for three different pulse energies of the 554 nm laser pulse, E_1 : 400 μJ (asterisks), 200 μJ (open circles), and 100 μJ (plus signs). In the top row (1a–1d), we show spectra for the fast electron signal, in which the Ba^+ core is left in the $6s^2S_{1/2}$ ground state. The data in the second row (2a–2d) corresponds to the slow electron signal, i.e., the final state of the Ba^+ is the $5d^2D_{3/2}$ or $5d^2D_{5/2}$ state. The bottom row (3a–3d) shows the branching ratio for the interaction, i.e., the fraction of ions that are in the ground $6s$ state. The four columns show data for detunings $\Delta_2 =$ (a) -6.99 , (b) -3.39 , (c) -0.95 , and (d) 0 cm^{-1} .

These differing spectra are manifested directly in the branching ratio for the ionization continua. The branching ratio also shows stronger intensity dependence when Δ_2 is large. For large Δ_2 , the depth of the branching ratio diminishes as the 554 nm laser intensity is lowered. One interesting observation in the branching ratio is that the profiles become symmetric as Δ_2 is tuned near zero. For $\Delta_2 = -0.95 \text{ cm}^{-1}$, for example, the ionization yields for the two channels are highly asymmetric but the branching ratio shows a nearly symmetric profile. From our data, we observe control of the branching ratio between 82% and 35%. Each of these limits is smaller than those from our previous study [7], possibly due to our current use of an improved detector.

An important parameter in modeling the interaction is σ_{6s}/σ_{5d} , the ratio of ionization cross sections into the $6s$ and $5d$ continua (commensurate to the branching ratio) from each of the intermediate states individually. In order to measure this ratio, we collect electron images when only one excitation channel is active at a time. Experimentally, we achieve this by keeping one of the lasers far detuned from resonance with the transition from the ground state. To measure the photoionization cross section from the $6s6p$ state, we tune the 554 nm laser to resonance ($\Delta_1 = 0$) and detune the 307 nm laser by $\Delta_2 = \pm 100 \text{ cm}^{-1}$ from the transition frequency from the ground state to the $6s7p$ state. We carry out this measurement twice, with the 307 nm laser tuned above and, alternatively, below resonance, in order to check the possible change in the cross section which could arise from structure in the continuum. Both measurements of σ_{6s}/σ_{5d} were within 3% of the average, indicating a flat continuum in

TABLE I. Relative ionization cross section.

σ_{6s}/σ_{5d}	via $6s6p$	via $6s7p$
Current study	6.27	1.33
Luc-Koenig <i>et al.</i> ^a	7.8	0.53

^aReference [9].

the region of our work. To measure the ratio of photoionization cross sections for the $6s7p$ state, we repeat the measurements with $\Delta_1 = \pm 100 \text{ cm}^{-1}$ and $\Delta_2 = 0$. Again the measurements above and below resonance yield consistent results within $\pm 3\%$. A flat continuum is expected here, as the nearest autoionizing resonances are the $6p7p \ ^1P_1$, the $6p7p \ ^3D_1$, and the $6p7p \ ^3D_2$ states, which lie 224 cm^{-1} below, 506 cm^{-1} above, and 595 cm^{-1} above the continuum state at energy ϵ , respectively [16]. The widths of the 1P_1 and the 3D_1 resonances are about 25 cm^{-1} , while that of the 3D_2 state is unreported.

Our measured cross-section ratios differ somewhat from the values previously calculated by Luc-Koenig *et al.* [9], as shown in Table I. These authors calculated these ionization cross sections several ways, using length and velocity gauges, and including or omitting correlation effects. They estimate that the uncertainties in their absolute cross sections are $\pm 20\%$. Variations of the ratios σ_{6s}/σ_{5d} that they report are significantly smaller, however. Our measured cross-section ratios, $\sigma_{6s}/\sigma_{5d} = 6.27$ and 1.33 , for the $6s6p$ and $6s7p$ intermediate states translate into branching ratios of 86% and 57% , respectively.

B. Measurements with delay pulse: Intermediate state population

We show a typical smoothed image that results from application of the delay pulse in Fig. 7(a). The bright central part of the image (inside the dashed guide line) corresponds to the signal from the $6s6p$ state (photoelectron kinetic

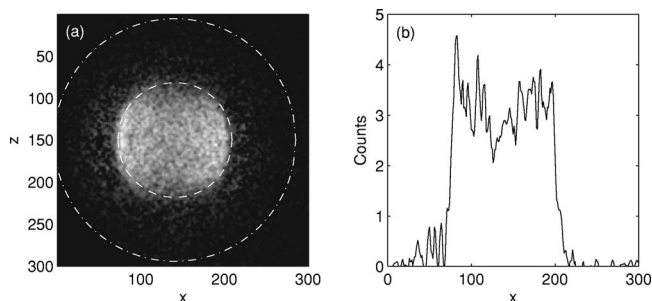


FIG. 7. Typical smoothed delay pulse image. In (a), we show an accumulated image in the x - z plane of the phosphor screen, while in (b) we show a single line (line 125) of these data. The bright central region inside the dashed white ring is the electron image from the $6s6p$ intermediate state, while the electrons ionized from the $6s7p$ intermediate state can be found within the outer dot-dashed white line on the figure. The detunings of the laser frequencies are $\Delta_1 = 0$ and $\Delta_2 = -3.39 \text{ cm}^{-1}$, and the pulse energies are $E_1 = 400 \mu\text{J}$ and $E_2 = 50 \mu\text{J}$ for this image.

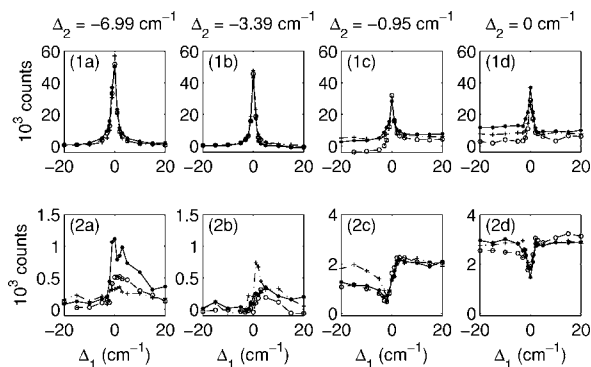


FIG. 8. Integrated delay signal via the $6s6p$ (1a–1d) and $6s7p$ (2a–2d) intermediate states. The symbols for the pulse energy of the 554 nm laser and the detunings Δ_2 are as given in Fig. 6.

energy = 0.52 eV), while the signal from the $6s7p$ state (kinetic energy = $2.32, 1.72, \text{ and } 1.62 \text{ eV}$) is distributed throughout the region inside the white dot-dashed guide ring drawn in the image. The delay pulse signal from the $6s7p$ state is much smaller than that from the $6s6p$ state, with the ratio of the electron yield as high as $60:1$. We show a single line trace of these smoothed data in Fig. 7(b). From these data, we derive a measure of the residual population of the two intermediate states by integrating over the area of the image and show these in Fig. 8. In the top row of this figure (1a–1d), we show the population remaining in the $6s6p$ state, determined by integrating within the inner (dashed) guide line in Fig. 7(a). In order to derive a measure of the residual $6s7p$ state population that is not masked by the much larger $6s6p$ signal, we integrate the photoelectron signal in the region between the guide lines only. We display these data in the second row (2a–2d) of Fig. 8. The general shapes of these spectra are clear and indicate that we have nearly symmetric population transfer to the $6s6p$ state with strong resonance behavior at $\Delta_1 = 0$, and asymmetric population transfer to the $6s7p$ state. The asymmetric profiles in the $6s7p$ signal follow the same asymmetric trend observed in the two-color signal, enhancement of ionization yield in $\Delta_1 > 0$ for negative detunings of the 307 nm laser, $\Delta_2 < 0$.

The peak amplitude of the $6s6p$ delay signal is independent of the 554 nm laser intensity, indicating strong saturation on $6s^2 \rightarrow 6s6p$ transition, as expected. The linewidths of these spectra are only about 2 cm^{-1} , however, and show no evidence of power broadening. While this observation seemed contrary to our initial expectations, it is, in fact, consistent with the results of numerical simulations, as we will discuss in Sec. V. These simulations will also highlight the distinction between the residual intermediate state population, as measured here, and the same population during the interaction of the atom with the two-color laser field.

C. PAD analysis

We now describe our analysis of the PAD data to explore what these data can reveal about the interaction. As a preliminary measurement, we first examine the angular distribution for each pathway individually. We implement this by tuning first one of the laser frequencies far from resonance

TABLE II. PAD amplitudes for photoionization via singly resonant interactions. The amplitudes A_0 – A_4 describe the photoelectron angular distribution for ionization into the $6s$ core state, while B_0 – B_4 describe the $5d$ core state. For each, we list the amplitudes for excitation through the $6s6p$ and $6s7p$ intermediate state. See Eq. (3) for explicit definition of these amplitudes. All entries in this table normalized to A_0 for the $6s6p$ intermediate state.

	A_n		B_n	
	$6s6p$	$6s7p$	$6s6p$	$6s7p$
$n=0$	1.000	0.322	0.115	0.348
$n=2$	1.038	−0.093	0.030	0.241
$n=4$	0.096	−0.018	0.008	0.007

($\pm 100 \text{ cm}^{-1}$) with the intermediate state, then the other. We list the amplitudes A_n and B_n in Table II for the excitation through the $6s6p$ and $6s7p$ intermediate states. The differences in the PAD amplitudes for each continuum channel are striking. The fast photoelectrons through the $6s6p$ intermediate state have a strong $\cos 2\theta$ component (A_2), comparable to the A_0 amplitude. On the other hand, the fast photoelectrons from the $6s7p$ state have a much more isotropic distribution, with $|A_2| \sim 0.3A_0$, and A_4 even smaller. For the slow photoelectrons the situation is reversed. The PAD through the $6s7p$ state contains a significant $\cos 2\theta$ component, while the dc component is dominant through the $6s6p$ state. It is interesting that we do not observe any significant $\cos 4\theta$ terms, which can correspond to a d -wave, and which could reasonably be expected to appear.

When we tune both frequency components of the field near their respective resonant frequencies, we observe the variation of the PAD with Δ_1 . We show the variation in the amplitudes A_0 , A_2 , B_0 , and B_2 in the two-color signal for fast and slow electron signals in Fig. 9. In the upper row (1a–1d), we show A_0 (asterisks) and A_2 (open circles) for the fast electron signal, while in the bottom row (2a–2d), we show

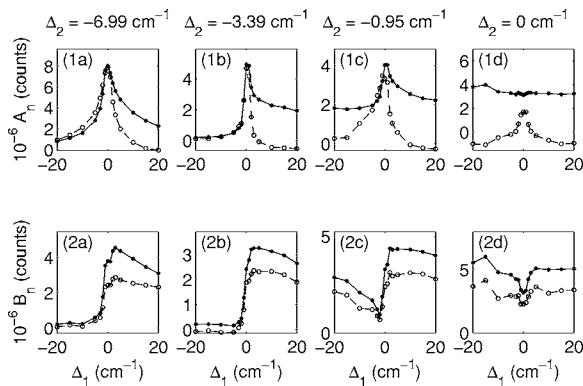


FIG. 9. The Fourier amplitudes when both fields are nearly resonant. In (1a–1d), we show A_0 (asterisks) and A_2 (open circles) for excitation of the $6s$ core state as a function of detuning Δ_1 . In (2a–2d) we show B_0 (asterisks) and B_2 (open circles) for excitation of the $5d$ core state. The pulse energies of the 554 and 307 nm beams are $E_1=400 \mu\text{J}$ and $E_2=50 \mu\text{J}$, respectively, for these data sets.

the amplitudes B_0 and B_2 . For both data, the dc components are usually, but not always, dominant. In the fast electron spectra, the amplitude of the $\cos 2\theta$ term is significant only near $\Delta_1=0$, and is much more symmetric in shape than the other terms.

We wish to explore the question of how these angular distributions can yield information about the role of interference in this interaction. Specifically, we would like to understand to what extent we can describe the partial ionization yields into the $6s$ and $5d$ channels simply in terms of the incoherent sum of ionization by way of the $6s6p$ state and ionization by way of the $6s7p$ state. For this purpose, we define the following partial ionization yields, each a term within Eqs. (1) and (2),

$$R'_{1,6s} \equiv \int_{-\infty}^{\infty} \{\gamma_{1,6s}^{\text{coh}} \sigma_{11}\} dt', \quad (4)$$

$$R'_{2,6s} \equiv \int_{-\infty}^{\infty} \{\gamma_{2,6s}^{\text{coh}} \sigma_{22}\} dt', \quad (5)$$

$$R'_{1,5d} \equiv \int_{-\infty}^{\infty} \{\gamma_{1,5d}^{\text{coh}} \sigma_{11}\} dt', \quad (6)$$

$$R'_{2,5d} \equiv \int_{-\infty}^{\infty} \{\gamma_{2,5d}^{\text{coh}} \sigma_{22}\} dt'. \quad (7)$$

To estimate the magnitude of these terms, we can make use of the coefficients A_2 and B_2 , in that A_2 for the $6s6p$ pathway dominates that of the $6s7p$ pathway, and for B_2 , the $6s7p$ contribution is much greater than that of the $6s6p$. Therefore, even if an interference between the amplitudes for the two pathways were present, the amplitude of the $\cos 2\theta$ component should be relatively insensitive to this effect, and a measurement of these amplitudes can serve as an indication of the relative magnitude of each pathway for the interaction with the two-color laser pulse. We will therefore use A_2 reported in Table II as a measure of the ionization rate through the $6s6p$ intermediate state into the $6s$ channel, and B_2 of that same table for the ionization rate through the $6s7p$ intermediate state into the $5d$ channel. We must appropriately scale these terms in order to yield the partial ionization probabilities we seek. For this we use $R_{6s}=4\pi(A_0-A_2/3-A_4/15)$ and $R_{5d}=4\pi(B_0-B_2/3-B_4/15)$, which are determined by integrating the angular distribution, $R_i = \int P_i(\theta, \phi) d\Omega$. Using this and the ratio of cross sections σ_{6s}/σ_{5d} discussed previously, and ignoring A_4 and B_4 , we estimate

$$R'_{1,6s} \approx A_2(\Delta_1) \frac{A_0 - A_2/3}{A_2} = 0.63A_2(\Delta_1), \quad (8)$$

$$R'_{2,6s} \approx B_2(\Delta_1) \frac{B_0 - B_2/3}{B_2} \times \frac{\sigma_{6s}}{\sigma_{5d}} = 1.11(1.33)B_2(\Delta_1), \quad (9)$$

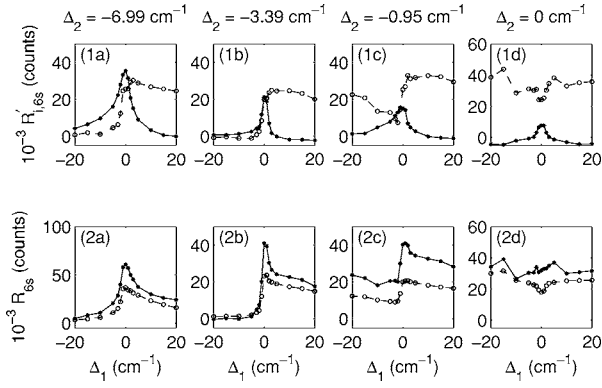


FIG. 10. Estimates of the ionization rate into the $6s^2S_{1/2}$ state of the Ba^+ core as determined from the photoelectron angular distribution data. In (1a–1d), we show estimates of the ionization rate by way of the $6s6p$ intermediate state, $R'_{1,6s}$ (asterisks) and through the $6s7p$ intermediate state, $R'_{2,6s}$ (open circles). In the bottom row, (2a–2d), the data points (asterisks) show the sum of these two terms, $R_{6s} = R'_{1,6s} + R'_{2,6s}$. For comparison, we reproduce the results of our measurements (open circles), reproduced from Fig. 6 (1a–1d).

$$R'_{1,5d} \approx A_2(\Delta_1) \frac{A_0 - A_2/3}{A_2} \times \frac{\sigma_{5d}}{\sigma_{6s}} = \frac{0.63}{6.27} A_2(\Delta_1), \quad (10)$$

$$R'_{2,5d} \approx B_2(\Delta_1) \frac{B_0 - B_2/3}{B_2} = 1.11 B_2(\Delta_1). \quad (11)$$

We show these estimates of $R'_{1,6s}$ and $R'_{2,6s}$ in Fig. 10 (1a–1d) as the asterisks and open circle data points, respectively, and the sum of these two terms in Fig. 10 (2a–2d) as the asterisks data points. In Fig. 10 (2a–2d), we have also reproduced the experimental data for the partial ionization yield for the fast electron signal from Fig. 6 as the open circles. From this comparison, it can be seen that our reconstruction of the total ionization signal for the fast electrons using the incoherent sum of the signals via the $6s6p$ and $6s7p$ intermediate states is only fair, reproducing the correct general shape of the spectrum, but missing the correct amplitude (for the case of one detuning) by up to a factor of 2. The model appears to be much better for the $5d$ channel. We show $R'_{1,5d}$ and $R'_{2,5d}$ in Fig. 11 (1a–1d). The sums of these two curves, shown in Fig. 11 (2a–2d), as asterisks, are in very close correspondence with the measured slow electron yield, reproduced in this plot as the open circles.

The calculated ionization yield in these figures does not include any interference effect, simply the sum of ionization yield from each pathway, yet the estimate of the slow electron signal agrees well with the ionization yield through two-pathway excitation in the experiment, and the agreement for the fast electron signal is fair. These PAD data indicate, therefore, that under the parameters of our measurements, an ionization model that ignores coherence terms works reasonably well. Deviation from the experimental value can be observed, but the deviation is mostly of a scaling factor that could arise from the uncertainty in the photoionization cross section or the deviation in the ratio of harmonic amplitudes

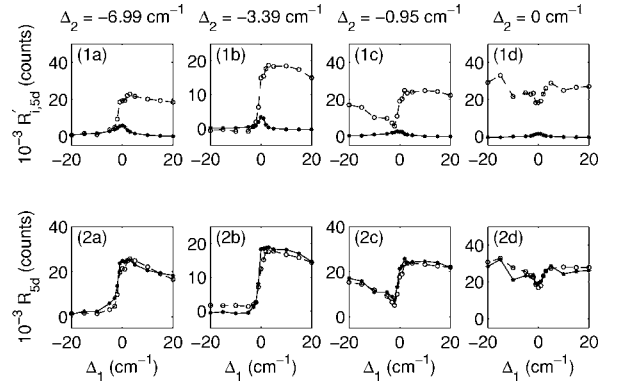


FIG. 11. Estimates of the ionization rate into the $5d^2D_J$ states of the Ba^+ core, for $J = \frac{3}{2}$ and $\frac{5}{2}$, as determined from the photoelectron angular distribution data. In (1a–1d), we show the ionization rate by way of the $6s6p$ intermediate state, $R'_{1,5d}$ (asterisks), and through the $6s7p$ intermediate state, $R'_{2,5d}$ (open circles). In the bottom row, (2a–2d), the data points (asterisks) show the sum of these two terms, $R_{5d} = R'_{1,5d} + R'_{2,5d}$. For comparison, we reproduce the results of our measurements (open circles), reproduced from Fig. 6 (2a–2d).

measured from a single pathway. We do not expect that an interference effect can be responsible for the deviation between model and measurement, as the deviation does not have the frequency dependence that one would expect to see in interference. The latter would be an odd function of Δ_1 , in contrast to the deviation between the curves in Figs. 10(b) and 11(b).

V. NUMERICAL SIMULATION

Our experimental procedures provide us with a set of physical measurements, such as residual intermediate population σ_{ii} . In order to better understand these results, we performed a series of numerical simulations following the procedure used by Nakajima *et al.* [8] in their study in calcium. Except for the ionization rates in Table III, we used the atomic parameters provided by Luc-Koenig *et al.* in Table 1 of Ref. [9]. We modified the ionization rates so that they matched our relative ionization cross sections listed in Table I, and produced ionization spectra for the $6s$ channel that matched our observed spectra. The dynamics of the system are governed by the coupled differential equations (3)–(6) in Ref. [8], and we follow the time evolution of these equations of motion under application of a pulsed laser input. We performed a numerical integration using a 5 ns duration (FWHM) \cos^2 -shaped laser pulse whose peak intensity of

TABLE III. Ionization rates used in our numerical simulations.

$\gamma_{1,6s}^{coh}$	$2 \times 16.82 I_2 \text{ cm}^2/\text{Ws}$
$\gamma_{1,5d}^{coh}$	$2 \times 2.67 I_2 \text{ cm}^2/\text{Ws}$
$\gamma_{2,6s}^{coh}$	$2 \times 5.17 I_1 \text{ cm}^2/\text{Ws}$
$\gamma_{2,5d}^{coh}$	$2 \times 3.88 I_1 \text{ cm}^2/\text{Ws}$

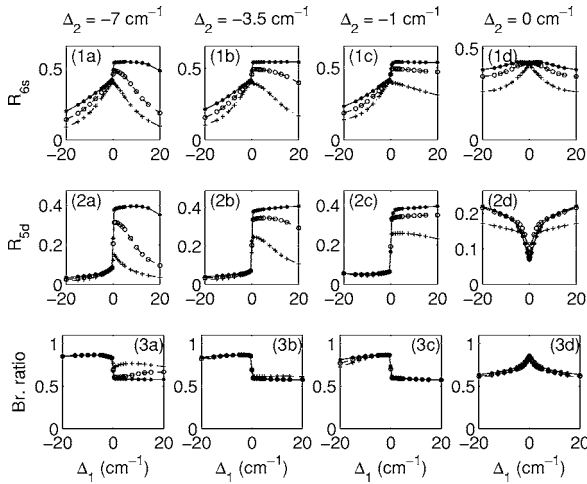


FIG. 12. Simulated spectra for first row (1a–1d): fast electrons, $6s$ core state; second row (2a–2d): slow electrons, $5d$ core state; third row (3a–3d): branching ratio to $6s$ state. The detunings Δ_2 for each column are (1a–3a) -7.0 cm^{-1} , (1b–3b) -3.5 cm^{-1} , (1c–3c) -1.0 cm^{-1} , and (1d–3d) 0 .

5.32×10^7 , 2.66×10^7 , or 1.33×10^7 W/cm^2 corresponds to the estimated peak intensity in the experiment for the 400, 200, and 100 μJ pulse energies for the 554 nm laser (I_1); 6.65×10^6 W/cm^2 corresponds to the 50 μJ pulse energy of the 307 nm laser (I_2).

The integration was carried out between a -12 ns $< t < 12$ ns time window, with the laser starting to turn on at $t = -5$ ns, peaking at $t = 0$, and completely turned off at $t = 5$ ns. Due to the high laser intensity and the large dipole transition moment, the Rabi frequency of the $6s^2 \rightarrow 6s6p$ was as high as 2.7×10^{12} s^{-1} , requiring extremely short step sizes in the integration process. As a result, some of the simulations took up to 2 h of CPU time on a PC for one scan of the 554 nm laser. To decrease the demands for computer time, we had to make a few simplifying assumptions. First, we did not include any spatial variation of the laser intensity. Intensity-dependent effects, which vary across the intensity profiles of the laser in the experiment, will therefore not be as pronounced as they are in the simulation. Also we have neglected several decay routes that could take place from the $6s7p$ state, and only considered decay from $6s7p \rightarrow 6s^2$ with the decay rate (5.3×10^7 s^{-1}) given in Ref. [9]. Consistent with our experimental geometry, we also assumed that the beams overlap one another perfectly, and that they are each of the same size.

We carried out our numerical simulations with several different 554 nm laser intensities, using the same Δ_2 as we used for the experiment, and show some of these results in Fig. 12. Results from the simulation show several spectral features similar to those that we observe in the experiment.

(i) The asymmetry in the fast and slow electron signals diminishes as the laser intensity decreases.

(ii) The slow electron signal retains a strong asymmetry for different 554 nm laser intensities.

(iii) The branching ratio is controlled, with high $6s$ to $5d$ channel ratio for $\Delta_1 < 0$.

The primary difference of these numerical results from the experimental data is in the fast electron spectra. Both

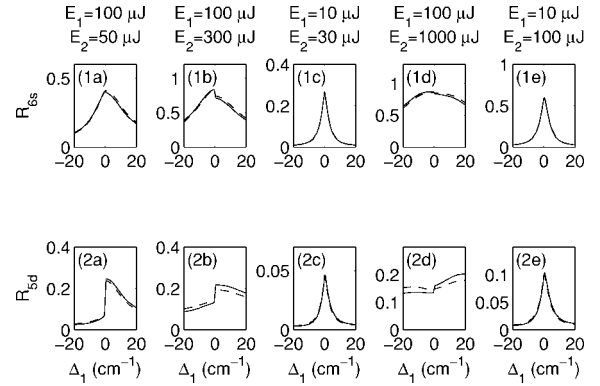


FIG. 13. Simulated spectrum for first row (1a–1e): fast electrons, $6s$ core state; second row (2a–2e): slow electrons, $5d$ core state. The detuning Δ_2 is -3.5 cm^{-1} for each plot, and the pulse energies E_1 for the 554 nm pulse and E_2 for the 307 nm pulse are given above each column. The solid line shows the spectrum when we include all terms, while the dashed line is the result when the interference term is turned off.

results show rather symmetric spectra, expected in the case of saturation by the intense field, although the linewidth is much broader in the simulation. This difference in linewidth could be a result of our approximation of a uniform spatial laser intensity profile. The maximum branching ratio in the simulation (87%) is consistent with our measurements (82%), while the minimum value (57%) is significantly higher than our observed value of 35%. The numerical results, of course, depend on the values used for atomic cross sections, decay rates, etc., and we have already noted some deviation in, for example, σ_{6s}/σ_{5d} between our measurements and the theoretical values of Ref. [9]. On the whole, however, the agreement between our measurements and the numerical studies is quite satisfactory.

In order to understand the effects of different processes, we repeated the simulation with the last two terms in Eqs. (1) and (2) set equal to zero. This effectively turns off the interference and allows us to determine the magnitude of its role on the total ionization signal. We found that under the conditions of our measurements, inclusion or omission of the interference terms has little impact, so we do not show separate spectra with the interference term turned off. We did use these simulations, however, in a search for intensities of the 554 and 307 nm pulses that might yield evidence of a more prominent role of interference. We show the results of this search in Fig. 13. From this figure, we can see that the interference is visible in the second and fourth columns, corresponding to $E_1 = 100$ μJ and $E_2 = 300$ μJ , and to $E_1 = 100$ μJ and $E_2 = 1000$ μJ , respectively. The pulse energies in column 3 are in the same proportion as in column 2, but interference is not visible in the former, indicating that saturating intensities, as well as balance between the Rabi frequencies, are necessary. This level of interference would be difficult to observe experimentally, and we did not attempt to generate UV pulses of the intensity that would be necessary to achieve this in the laboratory.

In order to understand these spectra more fully, we have plotted several simulated time-dependent quantities in Fig.

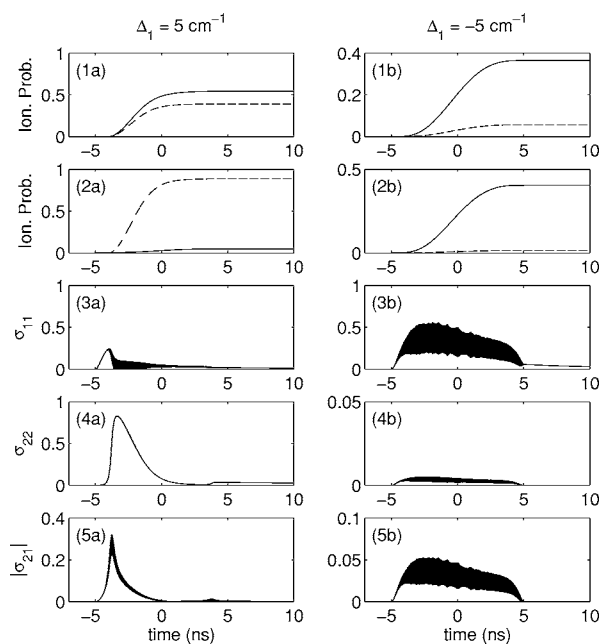


FIG. 14. Simulated time-dependent signals for pulse energies of $E_1=400 \mu\text{J}$ at 554 nm and $E_2=50 \mu\text{J}$ at 307 nm, and $\Delta_2=-3.5 \text{ cm}^{-1}$. Δ_1 is 5 cm^{-1} for the plots on the left (1a–5a), and -5 cm^{-1} for the plots on the right (1b–5b). In the top panel (1a and 1b), we show the ionization probability into the $6s$ channel (solid line) and the $5d$ channel (dashed). In the second panels (2a–2b), we plot the ionization probability through the $6s6p$ (solid) and $6s7p$ (dashed) intermediate states. Panels (3), (4), and (5) show the population of the $6s6p$ state, the population of the $6s7p$ state, and the coherence between these two states, respectively.

14 for pulse energies of $E_1=400 \mu\text{J}$ at 554 nm and $E_2=50 \mu\text{J}$ at 307 nm, and $\Delta_2=-3.5 \text{ cm}^{-1}$. Δ_1 is 5 cm^{-1} for the plots on the left (1a–5a), and -5 cm^{-1} for the plots on the right (1b–5b). In the top panel (1a and 1b), we show the ionization probability into the $6s$ channel (solid line) and the $5d$ channel (dashed). We see that the $6s$ channel signals are similar for the cases of $\Delta_1=5$ and -5 cm^{-1} , the major difference being that the signal arrives slightly earlier and reaches a somewhat higher level for $\Delta_1=5 \text{ cm}^{-1}$ than for $\Delta_1=-5 \text{ cm}^{-1}$. The slow electron signal, however, is significantly stronger for $\Delta_1=5 \text{ cm}^{-1}$ than for $\Delta_1=-5 \text{ cm}^{-1}$. In the second panels (2a–2b), we plot the ionization probability through the $6s6p$ (solid) and $6s7p$ (dashed) intermediate states. These simulated data show that most of the ionization is through the $6s7p$ state for $\Delta_1=5 \text{ cm}^{-1}$, but this pathway turns off and the $6s6p$ pathway turns on for $\Delta_1=-5 \text{ cm}^{-1}$. Panels (3), (4), and (5) show the population of the $6s6p$ state (σ_{11}), the population of the $6s7p$ state (σ_{22}), and the coherence between these two states ($|\sigma_{21}|$), respectively. For $\Delta_1=5 \text{ cm}^{-1}$, we can see a gradual population build-up in the $6s6p$ state as the laser pulse starts to turn on at $t=-5$ ns. At about $t=-3$ ns, the ac Stark shift has moved the ground state energy sufficiently that the $6s^2 \rightarrow 6s7p$ transition is resonant with the 307 nm laser, and we start to see population transferred to this latter state, with a concurrent increase in the coherence term. As the laser intensity continues to increase, however, the transition quickly shifts out of resonance, and

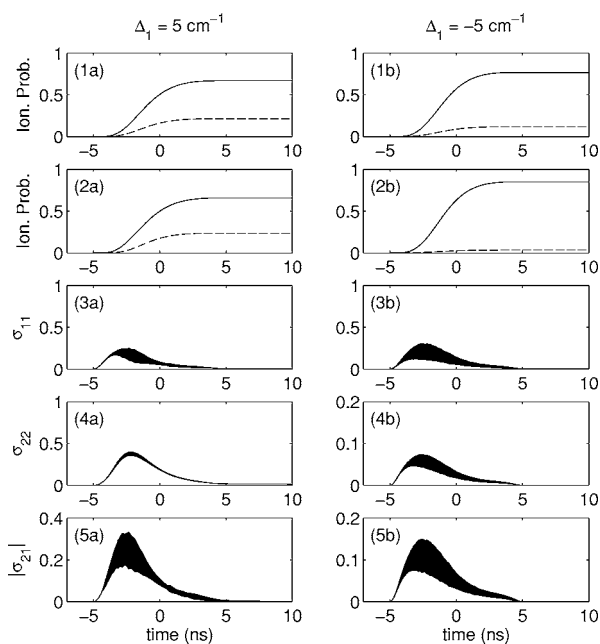


FIG. 15. Simulated time-dependent signals for pulse energies of $100 \mu\text{J}$ at 554 nm and $300 \mu\text{J}$ at 307 nm, and $\Delta_2=-3.5 \text{ cm}^{-1}$. The quantities shown are the same as in Fig. 14.

the population σ_{22} decays rapidly through ionization by the intense 554 nm laser. σ_{22} shows a small increase at about $t=3.5$ ns as the $6s^2 \rightarrow 6s7p$ transition is once again Stark shifted into resonance with the 307 nm laser pulse, but this population arrives too late to be ionized, so it slowly decays through spontaneous emission. Blackened areas on these plots indicate oscillation of the population or coherence term at the Rabi frequency.

For $\Delta_1=-5 \text{ cm}^{-1}$, the shift of the ground state moves the atomic transition away from resonance with the 307 nm laser, and very little population is transferred to the $6s7p$ state. While the coherence σ_{21} induced between the two intermediate states lasts a long time, its maximum amplitude is much less than it was for the case of $\Delta_1=5 \text{ cm}^{-1}$.

The dynamics of the atom are quite different when we change the pulse energies, bringing the Rabi frequencies of the two transitions into closer balance with one another. We show these simulated results in Fig. 15. For these simulations, we decreased E_1 to $100 \mu\text{J}$ and increased E_2 to $300 \mu\text{J}$, but kept the same laser detunings as in Fig. 14 [i.e., $\Delta_1=5 \text{ cm}^{-1}$ on the left side (1a–5a), $\Delta_1=-5 \text{ cm}^{-1}$ on the right side (1b–5b), and $\Delta_2=-3.5 \text{ cm}^{-1}$ throughout]. A key distinction of these curves is that the peak amplitude of the coherence term lasts longer than it did in the case shown in Fig. 14, and can therefore contribute more significantly to the net ionization signal. This coherence effect can be seen in Fig. 13 (1b) and (2b), where inclusion or omission of the coherence term in Eqs. (1) and (2) has a visible effect on the calculated ionization signal.

These time-dependent plots illustrate rather convincingly that the dominant factor in the control of the excitation of the ionization channel at the intensities that we used for our measurements is the ac Stark shift. This is further illustrated in Fig. 16, where we plot the ionization probabilities $R'_{1,6s}$

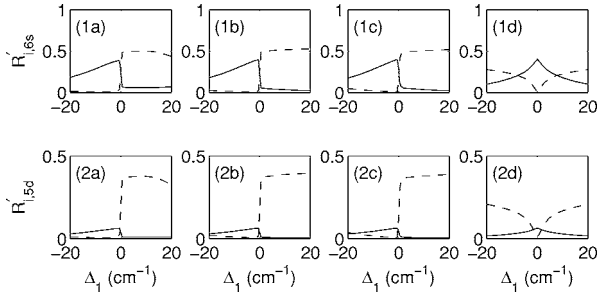


FIG. 16. Simulated spectra of $R'_{1,6s}$ and $R'_{2,6s}$ (1a–1d) and $R'_{1,5d}$ and $R'_{2,5d}$ (2a–2d). The solid and dashed lines represent ionization probabilities into the 6s and 5d channels, respectively. E_1 is 400 μJ , E_2 is 50 μJ , and Δ_2 is (1a–2a) -7.0 , (1b–2b) -3.5 , (1c–2c) -1.0 , and (1d–2d) 0 cm^{-1} .

(solid line) and $R'_{2,6s}$ (dashed line) in the top row (1a–1d), and $R'_{1,5d}$ (solid line) and $R'_{2,5d}$ (dashed line) in the bottom row (2a–2d). These calculated results show only the incoherent terms, but clearly indicate that, for $\Delta_2 \neq 0$, excitation of the 6s or 5d channel for $\Delta_1 < 0$ is predominantly through the 6s6p intermediate state, and for $\Delta_1 > 0$ is through the 6s7p state. Compare these spectra to the previous estimates from the data of $R'_{1,6s}$ and $R'_{2,6s}$ in the top row (1a–1d) of Fig. 10 and $R'_{1,5d}$ and $R'_{2,5d}$ in the top row (1a–1d) of Fig. 11. We conclude from this analysis that control of the photoionization branching ratio is largely due to varying population of these intermediate states through the ac Stark shift and the large difference in the photoionization cross sections into the two channels.

Our final observation from the numerical simulations is in regards to the population of the intermediate states. From the time-dependent plots of Figs. 14 and 15, we see that σ_{11} and σ_{22} can vary rapidly during the course of the pulse. We also see that in some cases (but not the cases shown in Fig. 14 or 15) the populations may be driven to a different value at the very end of the pulse. The values of σ_{11} and σ_{22} at $t = 12 \text{ ns}$, therefore, may bear little resemblance to the values of these variables during the laser pulse itself. For comparison with our delayed pulse measurements, then, we show in Fig. 17 numerical results for the final state population of the 6s6p (solid lines) and 6s7p (dashed lines) states. The 6s6p population shows a narrow peak near $\Delta_1 = 0$, similar to our measured spectra. (See Fig. 8.) The 6s7p population also contains a sharp spike in several cases, but more generally has a broad asymmetric component. This latter feature is also similar to our measured spectra. A major difference between these calculated results and our observations is in the relative magnitude of the σ_{11} and σ_{22} signals. In our measurements, the σ_{22} signal was much smaller than the σ_{11} signal. The difference could be due to a number of nearby autoionizing resonances that could enhance the ionization cross section for the 6s6p state when ionizing with UV light at $\lambda = 355 \text{ nm}$. Time-dependent plots indicate that the curious dip in the 6s6p population for small negative Δ_1 is due to the population of this level being driven to zero just before the end of the pulse as the second component of the Rabi pair is resonantly excited to the 6s7p state. We do not observe this feature in our delay pulse measurements, perhaps because of

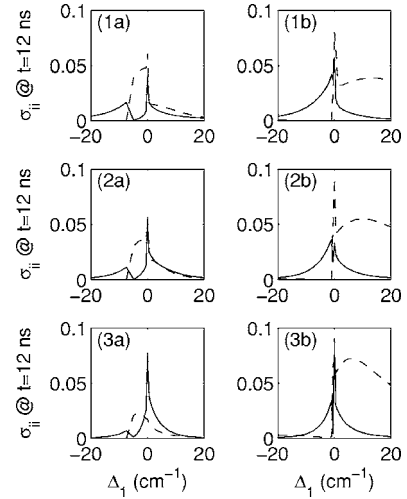


FIG. 17. Simulated spectra of σ_{11} (1a–3a) and σ_{22} (1b–3b) at $t = 12 \text{ ns}$. The solid and dashed lines represent population probabilities of the 6s6p and 6s7p intermediate states, respectively. The plots in (1a) and (1b) correspond to $E_1 = 400 \mu\text{J}$, (2a) and (2b) correspond to $E_1 = 200 \mu\text{J}$, and (3a) and (3b) correspond to $E_1 = 100 \mu\text{J}$. Detunings of the UV laser from resonance are $\Delta_2 = -7 \text{ cm}^{-1}$ for (1a)–(3a) and -1 cm^{-1} for (1b)–(3b).

the Gaussian spatial intensity profile of the laser beams. The residual population in the 6s6p state increases with decreasing intensity [compare Fig. 17 (3a) with (1a)] and, with the larger proportional area of the laser beam with increasing radius, this will dominate the signal.

VI. CONCLUSION

In the current work, the observed branching ratio between 6s and 5d core states ranged from 82% to 35%. These branching ratios are somewhat consistent with a model of photoionization taking place predominantly through the 6s6p intermediate state, for which the branching ratio is 86% when the signs of Δ_1 and Δ_2 are the same, or through the 6s7p intermediate state with a 57% branching ratio when the signs of Δ_1 and Δ_2 are opposite one another. While this observation does not defy the existence of an interference effect, we can conclude that the two-pathway interference does not provide further significant control of the branching ratio.

From the observation in the delay pulse signal and PAD analysis, we have identified the asymmetric population transfer to the 6s7p state as the main contribution to the asymmetric ionization spectra. The asymmetric population transfer to the 6s7p state results from the ac Stark shift, as discussed in Refs. [8,9].

The difference in Rabi frequency for the two resonant transitions from the ground state plays an important role in the peak asymmetries as well. In our measurements, the intensity of the 554 nm laser is much greater than that of the 307 nm laser, and the oscillator strength from the ground state to the 6s6p state is about three times larger than that for the transition to the 6s7p state. Overall the difference in the Rabi frequency is about an order of magnitude, which can reduce the coherence between the two intermediate states.

Numerical studies based on the model of Ref. [8] indicate that under different pulse energies, the effects of the interference on the ionization branching ratio can be increased. The key seems to be that the Rabi frequencies should be more closely matched, and strong saturation of the transition should be avoided. Still, the effect seems to be secondary in comparison to the role played by the Stark shift, and it would

be challenging to achieve the sensitivity that would be necessary to observe this.

ACKNOWLEDGMENT

This material is based upon work supported by the National Science Foundation under Grant No. 0099477.

-
- [1] B. Kohler, V. V. Yakovlev, J. Che, J. L. Krause, M. Messina, K. R. Wilson, N. Schwentner, R. M. Whitnell, and Y. J. Yan, *Phys. Rev. Lett.* **74**, 3360 (1995).
- [2] A. Assion, T. Baumert, M. Bergt, T. Brixner, B. Kiefer, V. Seyfried, M. Strehle, and G. Gerber, *Science* **282**, 919 (1998).
- [3] Doron Meshulach and Yaron Silberberg, *Nature (London)* **396**, 239 (1998); *Phys. Rev. A* **60**, 1287 (1999).
- [4] Paul Brumer and Moshe Shapiro, *Chem. Phys. Lett.* **126**, 541 (1986); *Faraday Discuss. Chem. Soc.* **82**, 177 (1986); Moshe Shapiro and Paul Brumer, *J. Chem. Phys.* **84**, 4103 (1986).
- [5] L. Zhu, V. Kleinman, X. Li, S. P. Lu, K. Trentelman, and R. J. Gordon, *Science* **270**, 77 (1995).
- [6] A. Shnitman, I. Sofer, I. Golub, A. Yogev, M. Shapiro, Z. Chen, and P. Brumer, *Phys. Rev. Lett.* **76**, 2886 (1996).
- [7] F. Wang, Ce Chen, and D. S. Elliott, *Phys. Rev. Lett.* **77**, 2416 (1996); F. Wang and D. S. Elliott, *Phys. Rev. A* **56**, 3065 (1997).
- [8] T. Nakajima, J. Zhang, and P. Lambropoulos, *Phys. Rev. Lett.* **79**, 3367 (1997).
- [9] E. Luc-Koenig, M. Aymar, M. Millet, J.-M. Lecomte, and A. Lyras, *Eur. Phys. J. D* **10**, 205 (2000).
- [10] H. Helm, N. Bjerre, M. J. Dyer, D. L. Huestis, and M. Saeed, *Phys. Rev. Lett.* **70**, 3221 (1993).
- [11] Zheng-Min Wang and D. S. Elliott, *Phys. Rev. Lett.* **87**, 173001 (2001).
- [12] Zheng-Min Wang and D. S. Elliott, *Phys. Rev. Lett.* **84**, 3795 (2000); Z.-M. Wang and D. S. Elliott, *Phys. Rev. A* **62**, 053404 (2000).
- [13] Ce Chen, Yi-Yian Yin, and D. S. Elliott, *Phys. Rev. Lett.* **64**, 507 (1990); Ce Chen and D. S. Elliott, *ibid.* **65**, 1737 (1990).
- [14] Yi-Yian Yin, Ce Chen, D. S. Elliott, and A. V. Smith, *Phys. Rev. Lett.* **69**, 2353 (1992).
- [15] L. O. Dicke and F. M. Kelly, *Can. J. Phys.* **49**, 2630 (1971).
- [16] P. Camus, M. Dieulin, A. El Himdy, and M. Aymar, *Phys. Scr.* **27**, 125 (1983).